Experimental and Numerical Study of Turbulent Flame Structures of a Spray Jet Flame

S Gallot-Lavallée, D Noh, W P Jones, S Navarro-Martinez, A Verdier, J Marrero Santiago, Gilles Cabot, Bruno Renou

Experimental and Numerical Study of Turbulent Flame Structures of a Spray Jet Flame

S. Gallot-Lavallée[1]*, D. Noh[1], W.P. Jones[1], S. Navarro-Martinez[1],
A. Verdier[2], J. Marrero Santiago[2], G. Cabot[2], B. Renou[2]
[1]Department of Mechanical Engineering, Imperial College London, London, UK
[2]Department of Experimental Combustion Analysis, CORIA - INSA, Rouen, France

Abstract
The flame structure of a laboratory scale *n*-heptane spray flame is investigated experimentally and numerically. The experimental burner is an open chamber with an ambient temperature co-flow surrounding a hollow cone simplex atomiser. OH-PLIF measurements are performed to study the interaction between turbulence, droplets, and chemistry. The simulation is performed using a Large Eddy Simulation with combustion modelling included by means of the solution of the transport of the joint-*sgs* probability density function using the stochastic fields method with promising results.

Introduction

Fundamental understanding of turbulent two-phase combustion is necessary because of its wide applications including gas turbines, internal combustion engines and industrial furnaces. A complete characterisation of the turbulent spray flame structures is still a difficult task from both experimental and numerical perspective. Spray flames involve several complex multi-scale phenomena, such as droplet evaporation, dispersion, and break-up through atomisation as well as the spray-flame and turbulence-chemistry interactions. In this prospective several experimental works are available analysing different combustion techniques such as Moderate Intense Low-oxygen Dilution (MILD) combustion, Exhaust Gas Recirculation (EGR), and Oxy-fuel combustion [1–4]. To overcome the limitation of the experimental works, many numerical studies have been performed in this field using both Reynolds Averaged Navier Stokes (RANS) [5] and Large Eddy Simulation (LES) [6–8]. The resolution of computationally very expensive primary atomisation is typically modelled and Lagrangian particles are used for the representation of the liquid phase. Different approaches to the atomisation process are available: empirically estimating a distribution of droplets and their velocities [8], assuming a distribution and using a conditional injection model [9, 10], or using a break-up model [11, 12]. The present work focuses on the study of the temporal evolution of spray flame structures and its stabilisation mechanisms by means of reliable experimental and numerical methods.

The experimental set-up consists of a spray jet flame stabilised on a burner equipped with a fuel atomiser producing a hollow-cone spray and a non-swirled air co-flow. This configuration is extensively characterised in the work from Verdier et al. [13]. Previous studies on the *n*-heptane/air lab-scale jet spray burner have shown that the flame exhibits a complex shape with a highly turbulent inner reaction zone and a quasi-laminar outer reaction zone. Here, additional measurements are included in terms of both mean and instantaneous OH fluorescence. Shum-Kivan et al. [14] performed an LES of the flame where a two step global reaction mechanism is used to model the oxidation of *n*-heptane. In the present work the numerical simulation is performed in the LES framework where the scalar fields are treated using a transported *pdf* approach. The solution of the joint sub-grid scale *pdf* is obtained by the Eulerian stochastic field method [15], which is used to represent the unknown influence of the small-scale fluctuations on chemical reactions. The dispersed phase is treated in a Lagrangian manner, and a stochastic break-up model is employed to minimise a priori parameters such as the droplet distributions at the inflow.

The present work is a combined experimental and numerical study of a canonical spray jet flame configuration. Quantitative comparison allows for the evaluation of the predictive capabilities of the LES. The global spray flame structure is discussed by means of both experimental results and numerical analysis.

Experimental Set-up

This section is dedicated to the description of the burner, the operating conditions and the optical diagnostics used for these experiments.

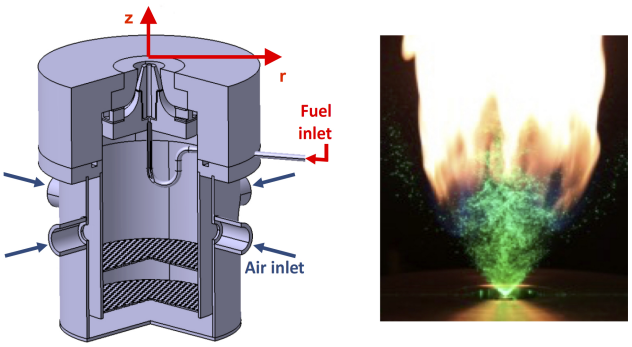

Figure 1: Detail of the injection system and typical flame picture when the flow is illuminated by a Nd:YAG laser sheet.

*Corresponding author: simon.gallot-lavallee@imperial.ac.uk

Burner and operating conditions:

Experiments are carried out in an atmospheric and open burner with a two-phase flow version of the KIAI burner [16]. The system is composed of a simplex pressure atomiser (Danfoss, $1.35[kg \cdot h^{-1}]$, 80° hollow cone) and an external annular non-swirling air co-flow with an inner and outer diameter of $10[mm]$ and $20[mm]$, respectively, refer to Fig. 1. Air and liquid fuel (*n*-heptane) mass flow rates are controlled by thermal and Coriolis mass flow controllers. The air and fuel inlet conditions are $6[g \cdot s^{-1}]$ ($T = 298 \pm 2[K]$) and $0.28[g \cdot s^{-1}]$ ($T = 298 \pm 2[K]$), respectively. The airflow leaves the annular pipe to enter the combustion chamber as a turbulent jet at a bulk velocity of $21.5[m \cdot s^{-1}]$. The airflow velocity has a great impact on the droplet distribution, segregating the droplets of different sizes and giving a spatial heterogeneous distribution along the chamber.

Optical diagnostics:

• *Phase Doppler Anemometry (PDA):* Droplet size and velocity are measured by a commercial PDA system (DANTEC) operating in DUAL mode. An argon laser provides green ($514.5[nm]$) and blue ($488[nm]$) beams. The beam spacing is $50[mm]$; transmitting and receiving lenses focal lengths are $350[mm]$ and $310[mm]$, respectively. Due to technical reasons, the off-axis angle of the receiving optics is 50° (in front scattering position), not far from the Brewster angle which, in parallel polarisation, enhances the refracted light detection over the reflected light, reducing the trajectory and slit effects. The laser energy before the beam separation in this work is set to $2[W]$. The aperture mask used allows for a detection diameter range of $139[\mu m]$. The measurement volume can be approximated by a cylinder with a diameter of $120[\mu m]$ and $200[\mu m]$ height. At each measurement position, data sampling is constrained to $40,000$ droplets or to $30[s]$ of the measuring time, allowing for converged statistics of size-classified data. Due to the spray structure and particle concentration distribution, it is not possible to perform measurements below $z = 7[mm]$. The gain and voltage in the photomultipliers (PMs) are adjusted to avoid the saturation of the anode currents in order to correctly detect the dispersed phase. The carrier phase velocity measurements are performed by seeding the air with $2[\mu m]$ olive oil droplets and increasing the gain and voltage in the PMs. The size and velocity of the dispersed phase (fuel spray) is measured in absence of the oil seeding.

• *OH Planar laser induced by fluorescence:* The two-phase flame structure is investigated by OH-PLIF imaging. White zones correspond to fresh gases, and the flame front is located at the interface between dark and white zones determined by the gradient on the image. An Nd-YAG-laser operating at $532[nm]$ is used to pump a tuneable dye laser (Quantel TDL90) supplied with Rhodamine $590[dye]$. The resultant output pulse energy is $30[mJ]$ per shot. The excitation wavelength is tuned to the $Q_1(5)$ transition of the $A^2\Sigma^+ (\nu' = 1) \leftarrow X^2\Pi (\nu'' = 0)$ band of OH at $\lambda = 282.75[nm]$. The collection system consists of an ICCD camera (PIMAX 4, Roper Scientific) equipped with UV lens ($f/2.8$). Background noise arising from elastic scattering by the droplets is reduced with a high-pass optical filter (Schott WG295) but is not completely eliminated so that droplets can be seen on the image. A broadband collection strategy from $308[nm]$ to $330[nm]$ with a band-pass filter (Schott UG11) is adopted.

Mathematical Modelling

Gas Phase:

The mass and momentum equations for low Mach number flows are spatially filtered in LES to separate the large resolved scales from the small modelled ones. Using the Favre filter or density filter, no modelling is required for the solution of the balance equation of mass. In the momentum equation unclosed terms results from the filtering operation and they represent the sub-grid-scales effects which are here regarded as an extra viscosity. The tensor τ_{ij}^{sgs} representing this viscosity is called sub-grid scale stress tensor, and is defined as $\tau_{ij}^{sgs} = \overline{\rho}_g \left(\widetilde{u_i u_j} - \tilde{u}_i \tilde{u}_j\right)$, and it is computed using the dynamically calibrated version of the Smagorinsky model by Piomelli and Liu [17]. The filtered forms of the conservation equations for the chemical species contain the filtered net formation rates through chemical reactions. Those are computed directly by the solution of the joint sgs-*pdf* evolution equation to determine species composition and energy. The modelled *pdf* equation is solved using the stochastic fields method [15] and further details can be found in [8].

Liquid Phase:

Fuel droplets are represented using the stochastic Lagrangian particle method described in [12, 18]. The size of droplets is assumed to be small compared to the LES filter width and they are therefore influenced both by the resolved and unresolved gas phase scales. The sub-grid scale fluctuations are modelled as a Markov process, i.e.:

$$d\mathbf{V}^{(i)} = \underbrace{\tau_p^{-1}\left(\widetilde{\mathbf{U}} - \mathbf{V}^{(i)}\right)\, dt + \left(1 - \frac{\rho_g}{\rho_\ell}\right)\mathbf{g}dt}_{deterministic} + \underbrace{\left(\frac{k_{sgs}}{\tau_t}\right)^{1/2} d\mathbf{W}_t}_{stochastic} \tag{1}$$

The equation for the velocity of the droplets is therefore characterised by a deterministic and a stochastic part. In the deterministic part $\mathbf{V}^{(i)}$ is the velocity vector of the i^{th} particle, $\widetilde{\mathbf{U}}$ the resolved gas phase velocity, ρ_g and ρ_l the densities of gas and liquid phase, respectively and $\mathbf{g}$ is the gravitational acceleration vector. The relaxation time for the particle is defined as $\tau_p^{-1} = \frac{3}{8} C_D \frac{\rho_g}{\rho_\ell} \frac{|\tilde{\mathbf{U}} - \mathbf{V}^{(i)}|}{r_p^{(i)}}$ where the drag coefficient is obtained from the Yuen-Chen law

[19], and r_p is the radius of the particle. The stochastic part is represented by the increment of a Wiener process $d\mathbf{W}_t$, k_{sgs} is the unresolved kinetic energy of the gas phase, and τ_t is the sub-grid time scale which modulates the dispersion rate introduced by the stochastic process. The before mentioned time constant is defined as:

$$\tau_t = \frac{\tau_p^{1.6}}{\left(\Delta/\sqrt{k_{sgs}}\right)^{0.6}} \tag{2}$$

The droplet evaporation is simulated using the well known Abramzon-Sirignano model [20] which assumes an homogeneous internal temperature distribution in the droplet and phase equilibrium conditions at the surface. Under these conditions the temperature $\Theta^{(i)}$ and mass $m^{(i)}$ of a single droplet i can be expressed as [21]:

$$\begin{aligned} d\Theta^{(i)} = &- \frac{\dot{m}_{(p)}}{m_{(p)} B_T'} \frac{C_{p_v}}{C_{p_\ell}} \left(\frac{\widetilde{\Theta}_g - \Theta^{(i)}}{\tau_p} \right) dt + \\ &\frac{h_v}{C_{p_\ell}} \frac{\dot{m}^{(i)}}{m^{(i)}} dt \end{aligned} \tag{3}$$

$$dm^{(i)} = -\frac{Sh^*}{3Sc_g} \left(\frac{m^{(i)}}{\tau_p} \right) \ln\left(1 + B_M\right) dt \tag{4}$$

where C_{p_ℓ} and C_{p_v} are the specific heat capacity of liquid and vapour, respectively, h_v is the latent heat of evaporation, B_T and B_M are, respectively, the heat and mass transfer Spalding numbers. The mixture properties are evaluated using the $1/3^{rd}$ rule. Nusselt (Nu^*) and Sherwood (Sh^*) numbers are modified such that they are the sum of a deterministic plus a stochastic term $\mathscr{A}^* = \mathscr{A}^{det} + \mathscr{A}^{sgs}$. This allows to include the effects of the unresolved fluctuation on mass and temperature evolution. The deterministic term is obtained by Clift et al. [22], while the stochastic contribution is:

$$\mathscr{A}^{sgs} = \mathscr{B}_g^{1/3} \left[\left(\underbrace{\rho_g \frac{k_{sgs}^{1/2} r_p^{(i)}}{\mu_g}}_{Re^{sgs}} \right) \frac{|d\mathbf{W}_t|}{dt^2} \right]^{1/2} \tau_p^{3/4} \tag{5}$$

where $\mathscr{B}_g$ is the gas phase Schmidt or Prandtl number as appropriate and μ_g is the gas phase viscosity.

Break-up model:

The break-up model used is proposed by Jones and Lettieri [12] and developed by Noh et al. [11]. The rate of change of the droplet number is described with a discrete Poisson process, the distribution of the droplet sizes originating from the breaking event is described by a *pdf* that varies depending on the turbulence intensity surrounding the droplet. The frequency of the occurrence of the break-up is determined by the value of $\omega(\epsilon, r)$ as a function of the radius and the dissipation of kinetic energy that is available in the context of LES by computing

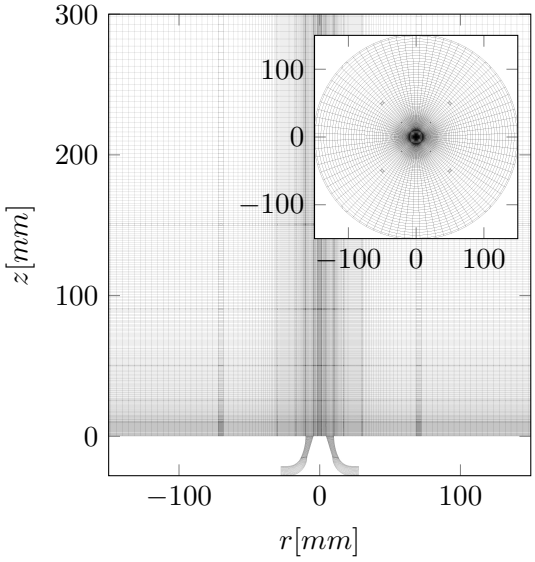

Figure 2: Computational domain used for the simulation. Section containing the centreline and orthogonal plane embedded in the former.

$\epsilon = 2\left(\mu + \mu_{sgs}\right) \tilde{S}_{ij} \tilde{S}_{ij}$.

$$\begin{aligned} \omega(\epsilon, r) = &\underbrace{K_g \frac{\sqrt{\beta \left(\epsilon 2r\right)^{2/3} - 12\sigma/(\rho r)}}{2r}}_{stochastic} + \\ &+ \underbrace{\frac{1}{\pi} \sqrt{\frac{8\sigma}{\rho_l (r)^3}}}_{deterministic} \end{aligned} \tag{6}$$

where σ is the surface tension of the liquid phase, and β has a value, according to Batchelor [23], of 8.2. The deterministic contribution to the break-up frequency is modelled to be the inverse of the break-up time scale [24]. The modelling of the stochastic part is based on the work from Martínez-Bazán et al. [25]. The model parameter K_g in the context of air bubbles was experimentally determined to be 0.25. The applicability of this methodology was extended to cases of liquid jets in gas [26]. The *pdf* of the size distribution of the *daughter* droplets $f(r, r_0)$ can be modelled as [25].:

$$\begin{aligned} &f^*(r^*) = \\ &= \frac{r^{*2} \left[r^{*2/3} - \Lambda^{5/3}\right] \left[\left(1 - r^{*3}\right)^{2/9} - \Lambda^{5/3}\right]}{\int_{r^*_{min}}^{r^*_{max}} r^{*2} \left[r^{*2/3} - \Lambda^{5/3}\right] \left[\left(1 - r^{*3}\right)^{2/9} - \Lambda^{5/3}\right] dr^*} \end{aligned} \tag{7}$$

where $r* = r_1/r_0$ and $\Lambda = r_c/r_0$. The critical radius $r_c = 2[12\sigma/(\beta\rho)]^{3/5} \epsilon^{-2/5}$ sets the threshold radius of the *mother* droplet r_0 for it to experience break-up. The break-up event is treated as a discrete Poisson release process in the interest of computational effort [12]. For further detail on the model and its implementation in this

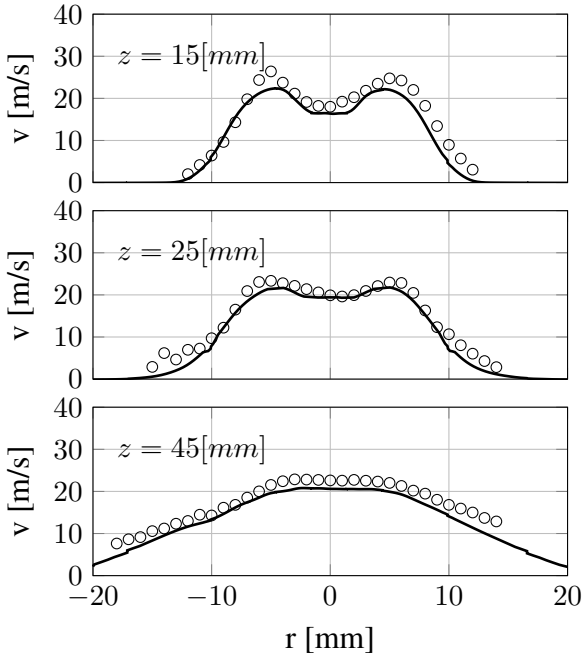

Figure 3: Mean axial velocity of the gas phase at different axial locations, both simulated (−) and measured (○) in reactive conditions.

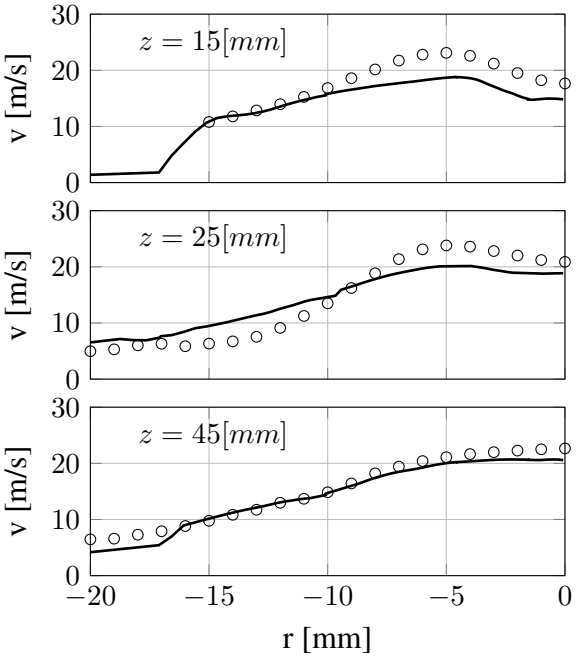

Figure 4: Mean axial velocity of the liquid phase at different axial locations, both simulated (−) and measured (○) in reactive conditions.

work refer to [11].

Numerical Set-up

The simulations are performed using the in house BOFFIN-LES code. A structured mesh is generated and reported in Fig. 2. It has cylindrical shape with $300[mm]$ height and $300[mm]$ diameter. It comprises 3 million cells divided into 158 blocks. The spacing of the grid is refined in the region of the atomiser with a minimum spacing of $0.13[mm]$ in the plane normal to the centreline that expands exponentially to $4.21[mm]$ in proximity of the outer radius. In the axial direction the spacing is set to be $0.2[mm]$ in the injection region expanding to $5.46[mm]$ at the furthermost downstream location. The expansion ratio between adjacent cells is constrained not to exceed 8% so that the commutation errors are negligible. The chemical scheme used for the *n*-heptane oxidation is the reduced mechanism involving 22 species and 18 reaction steps by Liu et al. [27]. The same mechanism is also used by Gallot-Lavallée et al.[8] in the BOFFIN-LES framework. The co-flow is simulated in order to reproduce the intrinsic turbulence generated by the experimental configuration.

Results

Flow field validation:

A comparison of the simulated and measured gas-phase velocity and dispersed phase average velocity is performed in reactive conditions. The gas phase axial velocity shows satisfactory agreement as it is observed in Fig. 3. The typical double peak in the velocity is caused by the presence of an annular co-flow which surrounds the injector. This feature dampens while proceeding towards downstream locations. Figure 4 shows the comparison of the mean velocity of the liquid phase where a good agreement is obtained. The intensity of the peak observed at $z = 15[mm], r = 5[mm]$ is not fully captured by the simulations and a possible cause for this is attributed to an over-prediction of the dispersion of big droplets reducing the momentum exchange.

Droplet size:

The comparison of the droplet size in terms of mean diameter ($d_{10} = \sum_{i=1}^{n} d_i/N$) is reported in Fig. 5 where the LES appears to globally over-predict the mean value. This could be caused by an under prediction of the break-up frequency which is currently being investigated. The small droplets deviate towards the centreline whilst the bigger ones behave ballistically, increasing the value of the d_{10} towards the edges of the jet. The effects of evaporation are evident by the decreasing value of the d_{10} at downstream locations. The results are promising and reliably reproduce the gas and liquid phase behaviour of the configuration.

Global flame structure:

In Fig. 6 the experimental and numerical profiles for the OH are presented together with an instantaneous snapshot of the droplets distribution. The instantaneous OH profile illustrates a vertical cross section of the double flame structure [4]. The overall shape of the flame exhibits two branches corresponding to an inner and an outer reaction zone sharing a common flame base.

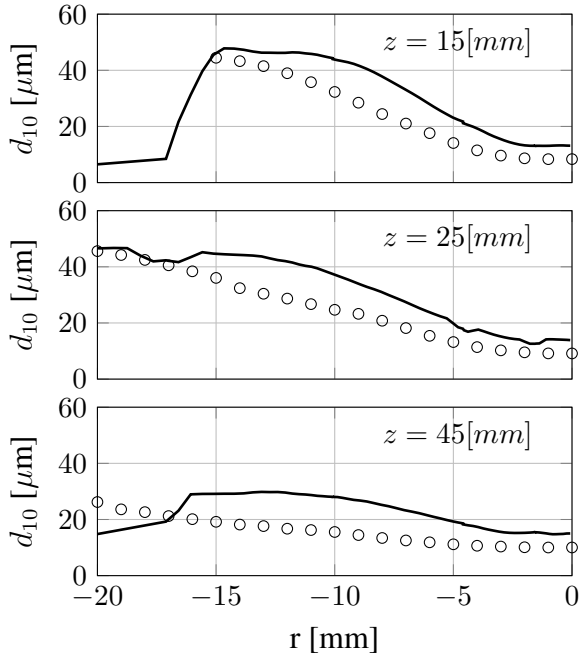

Figure 5: Mean diameter at different axial locations, both simulated (−) and measured (○) in reactive conditions.

The spray jet flame is lifted and stabilised around $r = 15[mm]$ and $z = 25 \pm 3[mm]$. The same feature in terms of OH production and lift-off height is observed numerically together with the fluctuation of the base which is due to the non homogeneous mixing of the fuel vapour. The flame front delimited by the OH profile is occasionally broken by the interaction with large droplets suggesting that this could contribute to the fluctuation of the flame. This flame structure results from the aerodynamics and spray heterogeneity in size [1], where the small droplets are mainly located in the centre and follow the air co-flow due to their low Stokes number. Large droplets spread into the outer part of the spray and follow more ballistic trajectories in Fig. 7 similarly to what is predicted numerically. The inner flame structure is strongly wrinkled and located along the shear layer created by the air co-flow discharging into the ambient air. Additionally, the inner flame is characterised by a strong OH gradient indicating that combustion occurs in a partially premixed regime with a flame propagation mechanism [14]. Fuel droplets are still visible in the vicinity of the inner reaction zone and are numerically observed to cross it. Those are predominantly large droplets that have enough mass and momentum to cross the flame front and and not fully evaporate. In the region between the flame fronts, where a weak OH trace is still visible, the high surrounding temperature, due to the combustion, imposes a fast droplet evaporation. The strong thermal exchange induces an augmentation of the gaseous fuel mass fraction. This fuel reservoir reacts further in the diffusion-like outer flame front. The outer reaction zone is less wrinkled, more stable, and thicker than the turbulent inner reaction zone, and characterised by a smoother OH gradient. This is also confirmed by the temperature profile presented in Fig 8 where the two flame fronts appear to be separated by a zone of lower temperature.

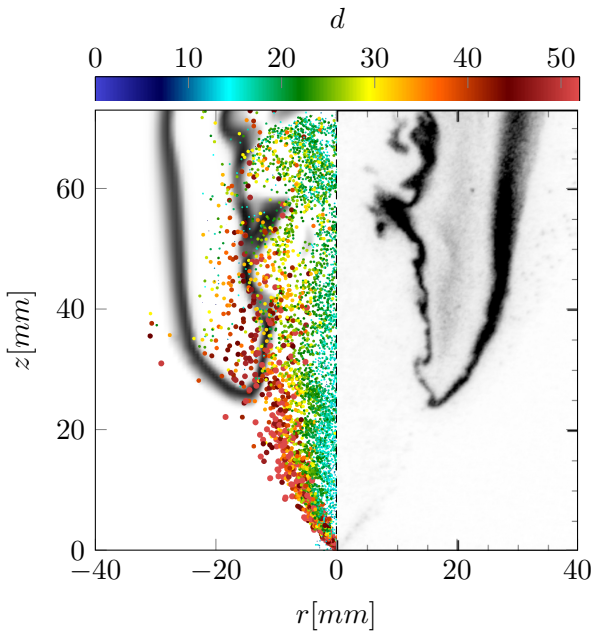

Figure 6: Instantaneous OH profile: LES (left) and OH-PLIF (right), together with a snapshot of the droplets scaled with their diameter.

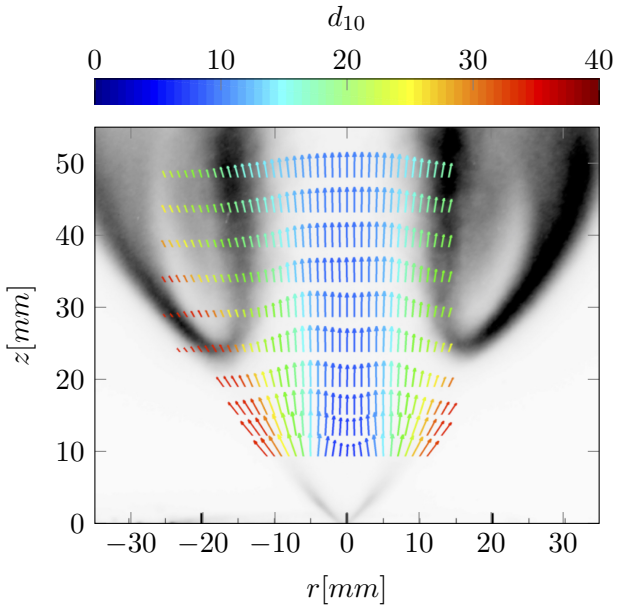

Figure 7: Mean OH-PLIF image with measured droplet velocity coloured by the droplet diameter.

Conclusions

A laboratory spray flame is investigated from a nu-

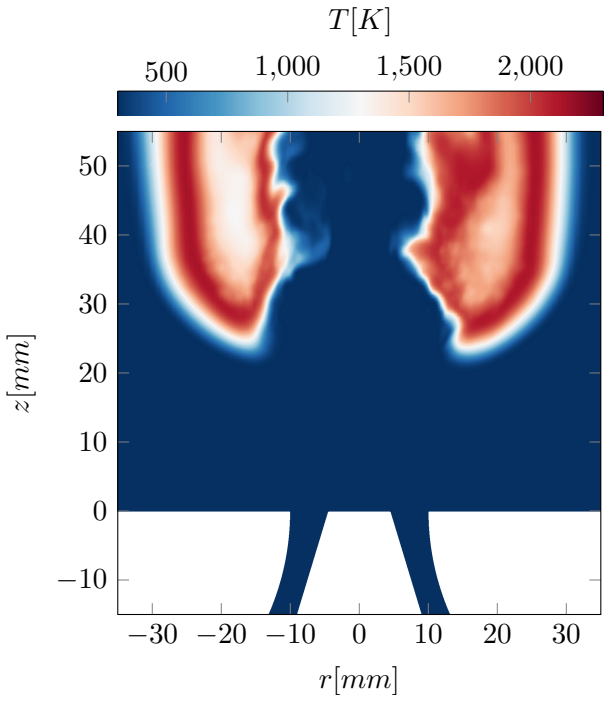

Figure 8: Instantaneous LES temperature distribution in a plane containing the centreline.

merical and experimental standpoint. Data relative to the velocities of gas and liquid phase as well as the droplet distribution are used as a benchmark for the numerical simulations. The analysis focuses on the flame structure and the stabilisation mechanism of the flame. The experimental data provided insight into the presence of two reaction zones. The internal one is characterised by high turbulence intensity and high OH gradients which are typical of the premixed regime. The external reaction zone is laminar and with a diffusion like OH profile. This observation is sustained by the information obtained numerically. Moreover the numerical simulation allowed for a further understanding of the interaction between the droplets and the flame front and their trajectories across the latter.

Acknowledgements

This work used the ARCHER UK National Supercomputing Service (http://www.archer.ac.uk). The authors gratefully acknowledge the financial support from the Agence Nationale de la Recherche with the TIMBER project TIMBER ANR-14-CE23-0009. Simon Gallot-Lavallée is grateful to General Electric Power (Switzerland) for their financial support.

References

[1] H. Correia Rodrigues, M. Tummers, E. van Veen, and D. Roekaerts. Int. J. Heat Fluid Fl. 51 (2015), 309–323.

[2] A. Kourmatzis, P. X. Pham, and A. R. Masri. Combust. Flame 162 (4) (2014), 978–996.

[3] M. Bardi, R. Payri, L. M. Malbec, G. Bruneaux, L. M. Pickett, J. Manin, T. Bazyn, and C. Genzale. Atomization Spray 22 (10) (2012), 807–842.

[4] G. Cléon, D. Honoré, C. Lacour, and A. Cessou. P. Combust. Inst. 33 (2014), 0–7.

[5] L. Ma, B. Naud, and D. Roekaerts. Flow Turbul. Combust. 96 (2) (2015), 469–502.

[6] L. Ma and D. Roekaerts. Combustion and Flame 172 (2016), 20–37.

[7] W. Jones, A. Marquis, and D. Noh. P. Combust. Inst. 35 (2) (2015), 1685–1691.

[8] S. Gallot Lavallée and W. P. Jones. Flow Turbul. Combust. 96 (2) (2016), 513–534.

[9] S Gallot-Lavallée, W. Jones, and A. Marquis. P. Combust. Inst. (2016).

[10] L. Ma and D. Roekaerts. Combust. Flame 165 (2016), 402–423.

[11] W. Jones, A. Marquis, and D Noh. P. Combust. Inst. (2016).

[12] W. P. Jones and C. Lettieri. Phys. Fluids 22 (11) (2010), 115106.

[13] A. Verdier, J. M. Santiago, A. Vandel, S. Saengkaew, G. Cabot, G. Grehan, and B. Renou. P. Combust. Inst. (2016).

[14] F Shum-Kivan, J. M. Santiago, A Verdier, E Riber, B Renou, G Cabot, and B Cuenot. P. Combust. Inst. (2016).

[15] W Jones and S. Navarro-Martinez. Combust. Flame 150 (3) (2007), 170–187.

[16] M Cordier, A Vandel, G Cabot, B Renou, and A. Boukhalfa. Comb. Sci. & Tech. 185 (3) (2013), 379–407.

[17] U. Piomelli and J. Liu. Phys. Fluids 7 (4) (1995), 893–848.

[18] M. Bini and W. P. Jones. J. Fluid Mech. 614 (2008), 207–252.

[19] M. C. Yuen and L. W. Chen. Comb. Sci. & Tech. 14 (1976), 147–154.

[20] W. Sirignano. Prog. Energy Combust. Sci. 9 (1983), 291–322.

[21] R. S. Miller, K. Hastard, and J. Bellan. Int. J. Multiphas. Flow 24 (1998), 1025–1055.

[22] R. Clift, J. R. Grace, and M. E. Weber. Courier Corporation (2005).

[23] G. K. Batchelor. Cambridge university press (1953).

[24] P. J. O'Rourke and A. A. Amsden. SAE (1987).

[25] C. Martínez-Bazán, J. Montanes, and J. C. Lasheras. J. Fluid Mech. 401 (1999), 183–207.

[26] J. C. Lasheras, C Eastwood, C Martınez-Bazán, and J. Montanes. Int. J. Multiphas. Flow 28 (2) (2002), 247–278.

[27] S. Liu, J. Hewson, J. Chen, and H. Pitsch. Combust. Flame 137 (2004), 320 –339.